Check for updates

Development of a bioactive, piezoelectric PVDF-TrFE scaffold with evaluation of tissue reaction for potential in nerve repair

Andrew E. Bryan,[a] Maksym Krutko,[b] Sandra Rebholz,[c,d] Lindsey E. Marquez,[b] Emma Busch,[a] Kevin Dong,[a] Sarah K. Pixley, [ID][e,h] Melanie T. Cushion,[c,d] Leyla Esfandiari [ID][b,f,g] and Greg M. Harris [ID] *[a,b,d,h]

Current biomaterials for trauma-associated tissue repair often fail to recapitulate the complex signaling environment required for effective integration and regeneration, particularly in modulating immune responses post-implantation. To address these limitations, we developed a multi-cue electrospun scaffold incorporating physiologically relevant chemical, electrical, and physical signals. Using blend electrospinning, we functionalized poly(vinylidene fluoride-trifluoroethylene) (PVDF-TrFE) with cell-secreted, decellularized extracellular matrix (dECM) to enhance cellular responses and limit foreign body reactions. The resulting scaffolds were systematically characterized *in vitro* for their structural, biochemical, and piezoelectric properties, and evaluated for their ability to support Schwann cell adhesion, metabolism, and repair-associated morphology in the context of peripheral nerve injury (PNI). *In vivo* subcutaneous implantation in rats demonstrated reduced foreign body giant cell formation at 7 days, and by 28 days, signs of regenerative healing, including vascularization and nerve tissue formation, were observed near the implantation site. Overall, these dECM-integrated PVDF-TrFE scaffolds effectively modulate immune responses and promote regenerative cell phenotypes. This work highlights the potential of bioactive, electroactive, and biomimetic scaffolds as next-generation implantable platforms for tissue engineering and repair.

1. Introduction

Peripheral nerve injuries (PNIs) caused by blunt or penetrating trauma, including motor vehicle accidents, sports injuries, combat-related incidents, and tumor resections, can result in pain, numbness, muscle weakness, and functional loss.[1]

[a]*Department of Chemical and Environmental Engineering, College of Engineering and Applied Sciences, University of Cincinnati, Cincinnati, OH, USA 45221. E-mail: gregory.harris@uc.edu; Fax: +(513) 556-3473; Tel: +(503) 556-4167*
[b]*Department of Biomedical Engineering, College of Engineering and Applied Sciences, University of Cincinnati, Cincinnati, OH, USA 45221*
[c]*Department of Internal Medicine, College of Medicine, University of Cincinnati, Cincinnati, OH, USA 45267*
[d]*Medical Research Service, Cincinnati Veterans Affairs Medical Center, Cincinnati, OH, USA 45220*
[e]*Department of Pharmacology, Physiology, and Neurobiology, College of Medicine, University of Cincinnati, Cincinnati, OH, USA 45267*
[f]*Department of Electrical Engineering, College of Engineering and Applied Sciences, University of Cincinnati, Cincinnati, OH, USA 45221*
[g]*Department of Environmental & Public Health Sciences, College of Medicine, University of Cincinnati, Cincinnati, OH, USA 45267*
[h]*Neuroscience Graduate Program, College of Medicine, University of Cincinnati, Cincinnati, OH, USA 45267*

Although peripheral nerves possess limited regenerative capacity, injuries involving gaps greater than a few millimeters generally require surgical repair.[2] The clinical gold standard, autologous nerve grafting, is constrained by donor nerve availability, the need for additional surgeries, donor site morbidity, neuroma formation, and limited success for nerve gaps exceeding a few centimeters.[3,4] To address these limitations, engineered biomaterials are being investigated as alternatives for nerve repair. Among these, electrospun scaffolds have emerged as promising candidates due to their ability to mimic the aligned architecture of native extracellular matrix (ECM), offering physical and biochemical cues that support cell attachment, migration, and axonal guidance.[5–8] Scaffold properties such as fiber alignment, stiffness, and surface chemistry are critical in modulating cellular behavior and directing regeneration.[9–13] Importantly, the ECM plays an active role in regeneration by providing dynamic reciprocity, which is bi-directional signaling between cells and their microenvironment that governs homeostasis and healing.[14–16] Materials that replicate this dynamic ECM environment are more likely to support functional regeneration. Our group and others have explored poly(vinylidene fluoride-trifluoroethylene) (PVDF-TrFE)

as an electrospun scaffold for nerve repair due to its piezoelectric properties.[17–23] These scaffolds enable the generation of local electric fields through mechanical deformation, which has been shown to enhance debris clearance, modulate Schwann cell behavior, promote neurite extension, and upregulate neurotrophic factors in nervous system regeneration.[24–34] Furthermore, electrical stimulation has also been shown to benefit skin and bone tissue repair.[35–37]

In addition to electrical and physical signaling, chemical properties of a biomaterial are vital for seamless integration within the body leading to clinical success.[38] For example, biochemical signaling is crucial in wound healing and occurs in PNS repair.[39–41] Despite its advantages, PVDF-TrFE lacks native cell-binding motifs, limiting its bioactivity. To address this, we developed a method that integrates decellularized ECM (dECM) from cultured cells into PVDF-TrFE scaffolds *via* blend electrospinning.[17] Compared to scaffolds functionalized with individual ECM proteins (*e.g.*, collagen, laminin), dECM more closely recapitulates the complexity and functionality of native tissue.[42,43] While singular components are all vital to the dynamic reciprocity occurring between the cells and ECM, a more relevant and physiological ECM is necessary to drive an appropriate regenerative response in PNS injury. The inclusion of dECM not only enhances cell adhesion and signaling but may also reduce inflammatory responses, a common challenge associated with synthetic implants.[44–47]

To address these challenges, we fabricated and characterized multi-cue, bioactive electrospun PVDF-TrFE scaffolds incorporating varying concentrations of dECM (Fig. 1). These scaffolds were evaluated for their chemical composition and tested both *in vitro* with primary cells and *in vivo* through subcutaneous implantation in rats as a preliminary study to ensure safety of the biomaterial. Our results demonstrate that the incorporation of dECM into electroactive PVDF-TrFE scaffolds improves biocompatibility, modulates immune responses, and promotes a regenerative microenvironment. This work shows great promise in the development of

advanced biomaterials for improving outcomes in PNI repair as well as general wound repair.

2. Materials and methods

2.1. Preparation of dECM

To produce dECM, NIH/3T3.2 fibroblasts (CRL-1658.2, American Type Culture Collection, Manassas, Virginia) were cultured and decellularized according to previously established methods.[48] In brief, cells were cultured at 1.38×10^4 cells per cm^2 in 150 mm tissue culture-treated polystyrene (Fisherbrand, Fisher Scientific, Waltham, MA) in a basal medium containing Dulbecco's Modified Eagle's Medium (DMEM) (Gibco) supplemented with 10% heat-inactivated bovine calf serum (BCS) (Cytiva, Marlborough, MA) and 1% penicillin/streptomycin (1×) (Gibco, Waltham, MA). Cells were maintained in a cell culture incubator at standard culture conditions for 7 days past confluence. Following culture, cells were washed twice with PBS, threefold with washing buffer and incubated in lysis buffer at 37 °C for 15 min. Lysis buffer was replaced with fresh buffer for an extended 60 min incubation period, washed three times with a final wash buffer. Wash buffer was replaced with PBS, dECM was scraped from the plate, and dECM with PBS was stored at −80 °C overnight to prepare for lyophilization. ECM was lyophilized using a 2.5 L Freezone Freeze Dry System (Labconco, Kansas City, MO). Dried ECM was enzymatically digested in a 0.01 N pepsin–HCl solution at room temperature for 48 h with the ECM : Pepsin ratio set at 10 : 1, as previously described by Freytes *et al.*[49] dECM mass values contained within this pepsin–HCl solution were used to quantify the mass : volume percentage of dECM contained in each electrospun scaffold.

2.2. Preparation of standard and bioactive PVDF-TrFE scaffolds

PVDF-TrFE resin (70/30) from PolyK Technologies (State College, PA) was prepared as detailed in our previous work.[18] Briefly, PVDF-TrFE resin was dissolved in a 6 : 4 volume–volume ratio mixture of *N*,*N*-dimethylformamide (DMF) and acetone at a 20% PVDF-TrFE weight to solvent volume ratio. Following dissolution, dECM solution was added to PVDF-TrFE solution and mixed thoroughly prior to blend electrospinning. When mixed, the solution was loaded into a 5 mL syringe fitted with a 20-gauge needle for electrospinning (Spinbox, Nanoscience Instruments, Phoenix, AZ) with the needle tip distanced 10 cm away from the rotating collector set to 2000 rpm. An 18 kV voltage was applied between the needle tip and collector and a sweeping motion was initiated with the needle and syringe. The solution was ejected from the needle at a rate of 1 mL h^{-1}. Following a spin time of 3 h, the aligned nanofibrous mat was removed from the collector and sectioned for use in experiments. Four types of PVDF-TrFE scaffolds with varying concentrations of dECM were blend-electrospun in this study: 0% dECM, 0.2% dECM, 0.3% dECM, and 0.4% dECM. These percentages were calculated as a mass :
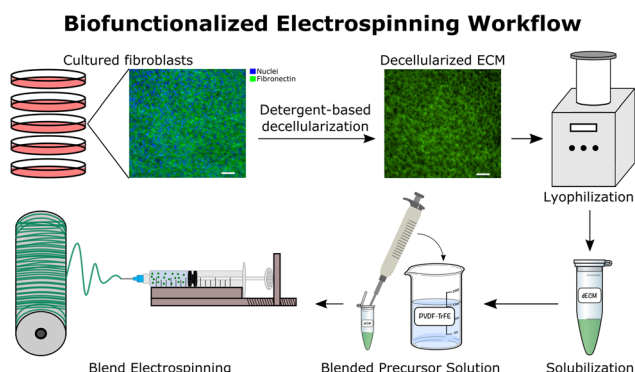

Fig. 1 Diagram of the preparation of scaffolds. Fibroblasts were cultured to produce abundant cell-derived ECM, then decellularized. ECM was collected, lyophilized, solubilized and added to a PVDF-TrFE solution. The blended precursor solution was electrospun into a spinning rotor to produce aligned scaffolds for testing.

volume ratio of dECM mass to PVDF-TrFE solution. To limit the variability in scaffold production, non-bioactive and biofunctionalized scaffolds were electrospun with the same parameters. Scaffolds functionalized with dECM were stored at 4 °C until used. Polycaprolactone pellets from Sigma-Aldrich (St Louis, MO) were electrospun into scaffolds with similar specifications (27-gauge needle, 14 cm needle-to-collector distance, 15 kV voltage, 1.5 mL h^{-1} flow rate, 2000 rpm collector, 3 h spin time).

2.3. Physical analysis of scaffolds

Fiber morphology was assessed using scanning electron microscopy (SEM), (ApreoC SEM, Thermo Fisher, Waltham, MA). Two samples of each scaffold type were sputter coated (Desk V, DentonVacuum) with a gold/palladium layer for 10 seconds (~1 nm). Five images per sample were taken at a 5 mm working distance and an acceleration voltage of 2 kV using an FEI XL-30 Philips microscope (Low-Vac). Fiber diameter and fiber alignment measurements were conducted using acquired SEM images in ImageJ software (version 1.52p), following established protocols.[50,51]

Scaffolds of each dECM percentage underwent tensile strength testing to determine bulk scaffold properties. Samples were cut into rectangular pieces sized 2 × 5 cm and analyzed using a universal testing machine (100R6; TestResources, Shakopee, MN). Scaffolds were stretched parallel to the direction of fiber alignment until failure at a rate of 1 mm min^{-1}. Using MtestWR software, force and displacement values were recorded to assess mechanical integrity and determine mechanical properties of each scaffold type. Given PVDF-TrFE is stable under normal physiological conditions, highly resistant to hydrolytic, enzymatic, and microbial degradation and is already a commonly used material in long-term biomedical applications, degradation studies were not performed.

dECM and control scaffolds were also analyzed using atomic force microscopy (AFM) (NanoWizard IV, JPK Instruments, Berlin, Germany). An AFM head with a silicon nitride cantilever (CSC37, k = 0.3–0.8 N m^{-1}, f = 20–40 kHZ, MikroMasch, Sofia, Bulgaria) was mounted on a fluorescence stereo microscope (M205 FA, Leica, Wetzlar, Germany) coupled with a Z-axis piezo stage (JPK CellHesion module, JPK Instruments). A sample slide was situated onto the AFM stage to record micrograph images in non-contact and Qi mode. Force–distance curves in a 10 × 10 μm square were measured from each nanofiber group under ambient conditions. The Young's moduli (E, Pa) of the nanofibers were determined by fitting the obtained force–distance curves with the modified Hertz model[52] and resulting stiffness values were analyzed (n = 100 per group).

2.4. Chemical and electrical analysis of scaffolds

To confirm the presence of dECM within blend-electrospun scaffolds, energy-dispersive X-ray spectroscopy (EDX) (EDAX, AMETEK, Berwyn, PA) was utilized to examine the ratio of carbon to fluorine in scaffolds. Spectra were recorded for each field of view and chemical composition was measured as a ratio of atomic percentages (Table S1 and Fig. S1). At least 5 images were measured from at least 3 different scaffolds per condition.

The crystalline structure of the scaffolds was assessed through X-ray diffraction (X'Pert Pro Diffractometer, Malvern Panalytical, UK). Samples were exposed to monochromatic CuK$_\alpha$ radiation at a scan rate of 0.013° s^{-1}, with 2θ values maintained between 15° and 43°.

Scaffolds were also evaluated using Attenuated Total Reflectance (ATR) Fourier transform infrared spectroscopy (FTIR) (Nicolet 6700 FTIR with Smart Orbit diamond ATR, Thermo Fisher) following methods previously described.[18] In short, the spectral range was configured to range from 4000 to 400 cm^{-1} with a resolution of 4 cm^{-1}. FTIR findings were engaged to quantify the percentage of the crystalline structure with the largest dipole moment, the β-phase, in each bioactive sample. Calculation methods relied on the assumption that absorption spectra adhere to the Lambert–Beer Law, which allows the estimation of the fraction of β-phase content to be estimated in a manner similar to methods described in Orkwis et al.[18]

To determine electric potential generated by the piezoelectric effect, PVDF-TrFE scaffolds comprising 0% dECM and 0.4% dECM groups were crafted into piezo-responsive chips. This was accomplished by cutting scaffolds into rectangular pieces sized 1.5 × 3 cm and situating a cantilever beneath the scaffold. The ends of the scaffold were affixed to a glass slide using a layer of conductive silver paint (Ted Pella Inc., Redding, CA) serving as an adhesive for electrodes. Opposing electrodes were connected to a ×10 voltage amplifier (Charge Amplifier for Piezo Sensor, Polyk Technologies, Philipsburg, PA), which was connected to an oscilloscope (Infiniium S-Series Oscilloscope, Keysight, Santa Rosa, CA) for voltage measurement (n = 6) in response to a mechanical stimulation. Stimulation was created by deforming the scaffolds using the installed cantilever. Deformed scaffolds underwent stimulation approaching ultimate tensile forces through maximum deformation to record measurable electrical signals. Captured signals were then filtered for analysis in MATLAB (The MathWorks, Inc. (2024b), ver. 24.2.0.2790852) followed by peak-to-peak electrical response calculation. Peak-to-peak voltage measurements were compared between 0% dECM and 0.4% dECM scaffolds.

2.5. Cell culture

Schwann cells were extracted from sciatic nerves of postnatal day 1–3 Sprague-Dawley rat pups (Charles River, Wilmington, MA). Whole nerve sections were cut into small pieces (2–3 mm) and placed in a pre-warmed trypsin-collagenase solution (2.5% : 1%) (Worthington Biochemical, Lakewood, NJ) for 30 min for tissue digestion. Sciatic nerve pieces were added to basal media, 10% Fetal bovine serum (FBS) from Cytiva (Marlborough, MA), and 2 mM GlutaMAX (Gibco), and centrifuged for 5 min at 50 rcf. The supernatant was discarded, and centrifugation was repeated. Immediately following, the super-

natant was decanted and fresh basal media supplemented with penicillin/streptomycin (1×) (Gibco) was added to the sciatic nerves. Trituration of the nerve pieces proceeded until no tissue fragments were visible. Cells were plated on 60 mm culture plates (Corning, NY) and incubated for 24 h under standard cell culture conditions to allow full adherence. Following incubation, cells were washed twice with Hanks Balanced Salt Solution (HBSS) and fibroblasts were removed *via* an anti-metabolic treatment. Briefly, basal media containing 10 µM Ara-C from Sigma-Aldrich (St Louis, MO) was added to cell cultures and incubated as above for 72 h. After culture, cells were washed 2× with HBSS and remaining fibroblasts were treated with anti-Thy-1.1 antibody (1 mg mL^{-1}) from BioRad (Hercules, CA) and rabbit complement serum (BioRad) for a duration of 30 min to 3 h to remove fibroblasts until near 99% purity of Schwann cells was achieved. Monitoring of this process occurred under a phase contrast microscope (Nikon Eclipse TE2000-U, Melville, NY) at 40× magnification. Upon fibroblast removal, basal medium supplemented with 10% FBS, forskolin (2 µM) from Thermo Fisher (Waltham, MA) and EGF-D (10 ng mL^{-1}) from R & D Systems (Minneapolis, MN) was added to the Schwann cell culture and cells were either placed in culture for experiments or frozen down for future use.

For *in vitro* studies, PVDF-TrFE scaffolds were partitioned into 1.5 × 1.5 cm squares and placed on 18 mm round coverslips (Fisher Scientific, Waltham, MA) in a 12-well, polystyrene culture plate (Corning, Fisher Scientific). Polytetrafluoroethylene (PTFE) rings sized 11 mm in diameter (Wilmad-Labglass, Vineland, NJ) were placed on top of each scaffold to ensure scaffolds did not float when culture media was added. Scaffolds were placed under UV light for 15 minutes followed by a 70% ethanol wash prior to experiments. Scaffolds were rinsed three times with sterile PBS following the ethanol wash. Primary Schwann cells were plated at a density of 26 000 cells per cm^2 on sterilized scaffolds.

2.6. *In vitro* scaffold assessment

An MTT (3-(4,5-dimethyl-2-thiazolyl)-2,5-diphenyl-2*H*-tetrazolium bromide) assay was used to monitor *in vitro* metabolism and serve as a surrogate for cell number. MTT powder (MilliporeSigma, Burlington, MA) was dissolved into PBS to form a 12 mM stock solution. For the assay, cells were plated and incubated for 3 h in the cell culture incubator. Following the 3 h culture time, media was aspirated and replaced with fresh DMEM. Then, the MTT reagent was added, and cells were further incubated for 2 h. Dimethyl sulfoxide (DMSO) was then added to each well to solubilize the MTT and the contents were mixed thoroughly before reading relative absorbance at 540 nm after 10 min (iMark, BioRad).

Cell alignment and aspect ratio were both quantified using microscopy images from fluorescein-phalloidin labeling. Briefly, primary Schwann cells were plated with a density of 10 000 cells per cm^2 on each scaffold type. Scaffolds were incubated in culture media for both 3 and 24 hours before undergoing fixation, permeabilization, and labeling. Twelve images of each scaffold type at each time point were taken with a

Nikon Eclipse Ti2 inverted microscope equipped with a Nikon DS-Qi2 camera and processed in ImageJ software. For cell alignment, following a method established for analyzing matrix alignment, images were processed using a fast Fourier transform analysis (FFT).[48] FFT images were analyzed, and intensity values drawn from the original image were normalized and plotted. Full width at half maximum (FWHM) values were computed and averaged across the twelve images of each scaffold type, then directly compared across all scaffold types. For aspect ratio, the ratio between the major axis length and minor axis length of each cell was calculated. At least three images per scaffold type per time point were analyzed.

2.7. *In vivo* implantation and tissue processing

A total of 32 Sprague Dawley adult rats were purchased from Charles River Laboratories and housed in the animal facility at Veterans Affairs Medical Center, Cincinnati, OH, USA. All surgeries and care for animals were conducted in AAALAC-accredited laboratories under the supervision of veterinarians. All procedures adhered to the regulations approved by the Institutional Animal Care and Use Committee of the Veterans Affairs Medical Center (Cincinnati, OH) and were in accordance with the guide for the Care and Use of Laboratory Animals (National Academies Press, Washington, DC, USA). Experimental groups consisted of electrospun scaffolds composed of PCL, PVDF-TrFE, and PVDF-TrFE + 0.4% dECM (5 rats per group) at 2 time points: 7 and 28 days.

Rats were anesthetized with isoflurane (4–5% induction, 1–3% maintenance) (Baxter Healthcare Corporation, Deerfield, IL). To prepare the surgical area of each rat, the dorsal midbody was shaved leaving an approximate skin area of 6 × 6 cm. This area was cleaned three times with alternating Betadine Scrub (McKesson Corporation, Irving, TX) and 70% alcohol (Thermo Fisher), then the rats were administered analgesics: Buprenorphine hydrochloride injectable at 0.1 mg kg^{-1} (Par Pharmaceutical, Chestnut Ridge, NY) and Meloxicam at 2 mg kg^{-1} (Covetrus, Portland, ME). Immediately following, a superficial incision was made to form a skin flap on the dorsal side proximal to the hip. A sterilized, dry scaffold piece size 1 × 1 cm was placed in the surgical opening and situated to avoid doubling. For ease of scaffold placement, large incision wounds were made. To minimize suture wounds affecting foreign body response measurements, ample space was ensured between the scaffold and incision. Wounds were sutured and animals were allowed to recover. Each scaffold group utilized 5 rats per time point.

On 7- and 28-days post-implantation (DPI), rats were euthanized by approved methods, shaved, and skin with attached mesh was harvested. Tissue samples were fixed in 10% formalin, placed in 70% ethanol, paraffin-embedded, and sectioned to be placed onto slides.

2.8. Immunofluorescent staining, microscopy, and image analysis

Sectioned tissue samples sliced at 4 µm were bake-dried at 60 °C for 20 min. After baking, slides were loaded onto a

Ventana Discovery Ultra system to be deparaffinized (3 cycles at 8 min each at 69 °C) and subjected to a mild EDTA-based antigen retrieval. Thereafter, slides were washed with DI water and dish soap and submerged in reaction buffer. Following this, tissue samples were tagged with immunofluorescent antibodies to quantify macrophage polarization. Recombinant rabbit anti-CD68 antibody (Abcam, EPR23917-164) was used for labeling M1-type macrophages. In adjacent sections, rabbit anti-mannose receptor antibody (Abcam, ab64693) was used to tag M2-type macrophages. A secondary antibody (anti-rabbit Alexa 594, Invitrogen, Waltham, MA, A11037) was used to label both M1 and M2 macrophages. Cells were then labeled using fluorescein phalloidin (Thermo Fisher, F432). All nuclei were labeled using DAPI (Abcam).

Fluorescent images were captured with a Nikon Eclipse Ti2 inverted microscope and a Nikon DS-Qi2 camera, using a 20× objective. Individual scaffold sections were stitched together to form whole-field scaffold images and the percentage of macrophages to total cells was measured in ImageJ. A threshold was applied to each image and a region of interest (ROI) was drawn around each scaffold to include the area of foreign body reaction. Each foreign body reaction area was visually characterized based on the number and arrangement of cell nuclei and their location adjacent to the surface of the implant. From this ROI, percentages of the area of macrophage stain to area of nuclei stain were measured at 7 and 28 DPI and presented in bar plots. Sets of measurements were performed by two separate investigators and averaged.

Adjacent sections were stained with hematoxylin and eosin (H&E) using standard procedures and mounted on a coverslip to be imaged. Images were captured with a Leica DMi8 Widefield Fluorescent microscope, using bright field optics, and a Leica MC170 HD microscope camera. Whole-field scaffold images were captured with a 40× objective and partitioned into at least three separate scaffold sections per animal. From these sections, one was chosen at random and at least 3 whole-field images were taken per chosen section, which resulted in 15 images per scaffold group for foreign body response analyses using two separate metrics. First, different aspects of the immune response to scaffolds were given a semi-quantitative histologic score adapted from Brown *et al.*[53] A list of the scoring criteria used for our study can be viewed in Table S2. Scoring involved identifying foreign body giant cells (FBGCs) and encapsulation. FBGCs are large immune cells formed by the fusion of macrophages in response to a foreign material. Their presence often indicates a negative foreign body reaction to the implant. FBGCs were counted only if it was clear that one cell contained multiple nuclei; nuclei were most often in a horseshoe pattern, suggesting that these could alternatively be designated as Langhans cells. Counting FBGCs provides a quantitative measure of the immune response and helps evaluate the biocompatibility of the material. Encapsulation refers to the formation of a fibrous tissue layer around the implant. This is a common outcome of the foreign body reaction and serves to isolate the implant from surrounding tissues. The thickness, compact-

ness, and density of collagen are used to measure the degree of tissue reaction (negative being more of each measure). Upon counting and identifying, each metric was given a number between 0 and 3. Higher scores were more indicative of a thinner, less dense capsule and therefore a constructive remodeling response. Lower scores suggested potential scar tissue or an adverse foreign body response. Scores were provided by two different investigators and averaged. To count FBGCs, a square grid was placed over each scaffold image with each square sized to the area of a 40× field of view of the microscope and camera system used to capture H&E images (309 μm × 235 μm). Squares were numbered from left to right starting in the top right corner. Beginning with square one, FBGCs were counted and continuing every fourth square thereafter assuming each square to be counted met the inclusion criteria. Inclusion criteria were determined such that for a square to be counted, it must include any portion of the area of inflammation and must contain at least 50% imaged tissue or scaffold. For this study, inflammation was defined as an influx of neutrophils and mononuclear macrophages subsequently followed by FBGCs surrounding the implant interface. If squares to be counted did not meet inclusion criteria, the square immediately to the right was selected until inclusion criteria were met. FBGCs were counted and averaged from a total of 5 images per scaffold type and given a score. For encapsulation, scores were given upon examining full-field scaffold images. A total remodeling score was then calculated as an average of combined metrics for each scaffold group. Scores with half values were rounded down to the nearest whole number. As an additional metric, FBGCs were numbered and calculated as a percent density to total number of cells surrounding the scaffold within the area of inflammation. A total of three fields of view were analyzed per tissue slice and five total tissue slices were analyzed per scaffold group. FBGC percentages for 7 DPI were presented in bar plots.

2.9. Statistics

Statistical analyses were performed using GraphPad Prism version 5.03 for Windows (Boston, MA), R (R Core Team, 2022), RStudio (RStudio Team, 2022) and the multcomp package (Hothorn, 2023). Significance values were set at $p < 0.05$. Statistics were evaluated using two-way analysis of variance (ANOVA) tests followed by a Tukey's *post hoc* comparison of all pairs of columns for cellular alignment and aspect ratio. A Bonferroni and Holm comparison was used for analyzing cell metabolic activity. All data is reported as a mean ± one standard deviation. XRD, FTIR, and tensile testing were all performed with n values of 3 scaffolds. Cell metabolic activity was measured with $n = 3$ separate wells per scaffold group and cell alignment was measured with $n = 12$ images per group. Cell aspect ratio was quantified with $n = 3$ images per group.

For *in vivo* measurements, macrophage percentages of immunofluorescent images at 7 days were quantified using at least $n = 13$ slides per group for M1 macrophages and $n = 7$ slides per group for M2 macrophages. Each slide included the entire scaffold piece in the field of view. Macrophages at 28

days underwent a qualitative analysis. For H&E images at 7 days, each scaffold image was partitioned into at least three sections. From this total number of sections per animal, three images were randomly chosen and quantified. Five separate scaffold images per chosen section were analyzed per scaffold grouping for a total of 15 measurements per group. H&E images obtained from scaffolds implanted for 28 days were qualitatively assessed. All animals were assessed for 7-day *in vivo* studies, but not all animals for 28 days due to an inability to locate scaffold when sectioning tissue slices. Outliers for all statistical measurements were calculated using a Grubbs' test and removed accordingly. Plots to represent quantified data were performed using GraphPad Prism.

3. Results

3.1. Mechanical characterization of bioactive scaffolds *via* blend electrospinning

Solubilized dECM was thoroughly mixed with PVDF-TrFE precursor solution to formulate blend-electrospun nanofibrous scaffolds of increasing dECM concentrations. Scaffolds with dECM concentrations ranging from 0%–0.4% displayed different morphological characteristics (Fig. 2A). dECM pre-sented as three-dimensional web-like structures dispersed throughout the scaffold, most visible in the 0.4% SEM image. The 0.4% scaffold group was the only group with fiber diameters approaching 2 microns and averaged fiber diameters much larger than any other group (Fig. 2B and C) with statistical differences existing between all other scaffold types. All other groups presented with much lower fiber diameters with no differences seen between 0% unaligned (UA), 0% aligned (AL), and the three dECM scaffolds (ANOVA, Tukey's *post hoc*, $p < 0.05$, $n = 3$ scaffolds per group).

Alignment indices varied for the differing scaffolds. The 0% dECM aligned (AL) scaffold (positive control) and 0.4% dECM group showed no differences in alignment. Both groups were statistically different from all other dECM groups and the 0% UA group (negative control) (Fig. 2D). Although statistically different from the positive control, the 0.2% and 0.3% scaffolds were not statistically different from unaligned fibers, suggesting some degree of alignment. Polar plots used to calculate alignment indices are presented in Fig. S2. While blended scaffolds were electrospun with identical collector parameters, the voltage and flow rate also affect fiber alignment.[54,55] The differences seen in 0.2% and 0.3% dECM scaffolds compared to aligned scaffolds could be caused by variations in these factors. Flow rate differences could occur
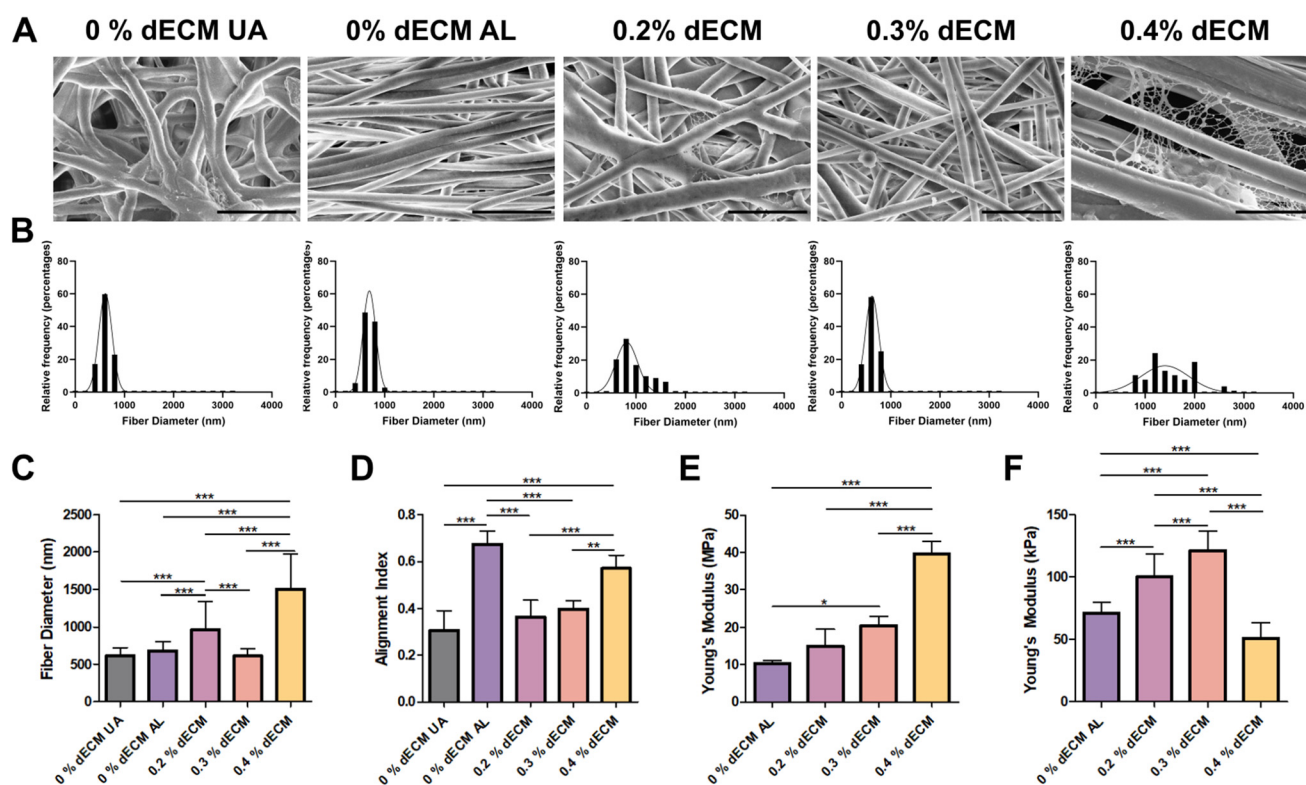

Fig. 2 Characterization of the physical and mechanical properties of scaffolds. (A) SEM images of the final scaffolds show fiber alignment and size with various dECM concentrations. These highlight visible dECM content as a coating and as webbing between fibers (scale bar = 5 μm). (B, C) Fiber diameter distribution and average diameter sizes of the scaffolds. (D) Alignment indices varied amongst all scaffold groups. (E) Young's modulus calculated from stress−strain curves at the macroscopic level exemplified forces the material would experience at a tissue-like level. (F) Young's modulus obtained from atomic force microscopy provides detailed material characterization at the atomic level giving insight into the potential forces cells might experience. All data are reported as mean ± SD. * $p < 0.05$, ** $p < 0.01$, *** $p < 0.001$.

amongst scaffold groups due to viscosity changes in the solution from the addition of water within the dECM solution. Further exploration of the effects of viscosity and water content on electrospinning could detangle this relationship.

Bulk mechanical properties were assessed on a tissue level scale *via* tensile tests and at a cellular level with AFM. Young's modulus was determined from the stress–strain curves produced by each respective test (Fig. 2E). 0.4% dECM scaffolds possessed the highest Young's Modulus which agrees with studies showing fiber diameter directly correlates with a change in total material stiffness.[56] Furthermore, its magnitude (39.6 ± 3.3 MPa) was the only one most closely associated with human peripheral nerve tissue magnitudes (~38 MPa).[57] Micro-level measurements using AFM nanoindentation showed Young's modulus increased from 0% to 0.3% groups. However, 0.4% scaffolds were significantly lower (51.4 ± 12.2) than all other scaffold groups (Fig. 2F). All pairs were significantly different from each other (ANOVA, $p = 0.05$, Tukey's *post-hoc* test).

3.2. Chemical and electrical analysis of functionalized scaffolds

EDX imaging was performed on the different scaffold groups to chemically confirm the presence of dECM on the surface of the blended scaffold groups. Composed purely of hydrogen–carbon–fluorine bonding, the spectrum obtained from imaging demonstrates peaks characteristic of carbon and fluorine atoms present (Fig. 3A). Additional quantification demonstrated the atomic percentages of each element within the sample. As a baseline, the atomic $C : F$ ratio in 0% PVDF-TrFE was approximately 1.5 (Fig. 3B). As biological material is heavily saturated with carbon, the incorporation of biological matter introduced more carbon matter into the scaffold. As expected, 0.4% dECM scaffolds contained more carbon to fluorine than controls, providing evidence our scaffolds contained biological content ($p < 0.001$).

The process of electrospinning PVDF-TrFE powder into nanofibrous scaffolds has previously been shown to enhance the piezoelectric potential of the final product in comparison to powder.[18] To ensure blend electrospinning did not alter the β-phase crystallinity of scaffolds, X-ray diffraction (XRD) patterns were collected. Patterns of each scaffold presented with strong diffraction peaks at $2\theta = 19.9°$ (Fig. 3C), corresponding to the (110) and (200) crystallographic planes of the β-phase structure of PVDF-TrFE, which suggests the addition of dECM prior to electrospinning does not alter β-phase crystallinity in blended scaffolds.[58,59]

To provide a more quantitative metric and individually address the amount of β-phase content in each scaffold type, FTIR spectra were obtained and the Lambert–Beer Law was applied to return content percentages (Fig. 3D). The 0% dECM and all blended scaffolds were in the range of 70 to 74 content percentage, with no significant differences between groups. These values are similar to findings from our lab with non-blended scaffolds,[17,18] further confirming that the piezoelectric capacity of the scaffolds is retained during the blend-electrospinning formulation process.

To quantify retained electrical output of blended piezoelectric scaffolds, rectangular scaffold pieces were sealed at each end to electrodes, then connected to an oscilloscope. The 0% aligned and 0.4% dECM scaffolds were repeatedly pulled from the center *via* a cantilever system, and corresponding electrical activity was recorded. Results showed a spike in signal when pressure was exerted and repeated signaling from periodic deformations were also seen (Fig. 3E and Fig. S3). Electrical activity from the 0% and 0.4% scaffold groups produced approximately 10 mV upon each surface deformation (Fig. 3E), and values were not statistically significant. The ability of the 0.4% dECM scaffolds to produce electric potentials equivalent to that of standard PVDF-TrFE scaffolds confirmed retention of electric potential following blend electrospinning.

3.3. *In vitro* cell–biomaterial interactions

Initial cellular attachment to scaffolds after 3 hours in cell culture medium was assessed *in vitro* using primary Schwann cells with metabolic activity assayed with an MTT colorimetric assay. Following a 3 h period of adhesion and growth, cells on 0.3% and 0.4% dECM scaffolds showed significantly increased MTT absorbance *versus* 0% scaffolds consistent with greater numbers of attached cells (Fig. S4).

Primary Schwann cells grown on bioactive dECM scaffolds were examined for morphology and growth at 3 h and 24 h. At 3 h, by visual examination (Fig. 4A), cells on 0.2% and 0.3% scaffolds looked less aligned and appeared to have fewer long processes than on 0% and 0.4% scaffolds. At 24 h, cells on all scaffold types visibly appeared to have lengthened morphologies in the direction of the aligned nanofibers (Fig. 4B). Cell alignment was quantified using image analysis as detailed in Harris *et al.*[48] All average FWHMs detailing alignment metrics were compared across groups and time points using a two-way ANOVA. Statistical differences were absent between time points, but present amongst scaffold groups within each time point. At 3 h, cell alignment was greatest on 0% scaffolds (average FWHM was lowest at 61.75 ± 1.35) and was significantly different from 0.4% (avg. 74.50 ± 5.24) (Fig. 4C and E). As indicated by the wider spreading cell shape, 0.2% scaffolds (avg. 82.58 ± 5.26) and 0.3% scaffolds (avg. 82.83 ± 3.48) possessed significantly less aligned indices than 0%, but were not different from 0.4%. At 24 h, cells on all scaffold types showed the same degree of aligned growth (Fig. 4D and E).

At an individual cell level, cell aspect ratios were measured at 3 h and 24 h and compared using a two-way ANOVA (Fig. 4F). Above, at 3 h, we showed that cells on 0% scaffolds were more aligned than any other group. Here cell aspect ratios of the 0.4% dECM group were the greatest at 3 hours of all groups, suggesting that the presence of greater amounts of protein improves cell aspect ratio. While the aspect ratio of cells on 0% scaffolds was greater than 0.2% dECM scaffolds, it was not different from 0.3% scaffolds. At 24 h, fewer differences were present. Scaffolds with 0%, 0.3%, and 0.4% dECM were not different from each other, but all three groups were different from 0.2% scaffolds. This suggests 0.2% dECM protein content is not a significant amount of protein to over-
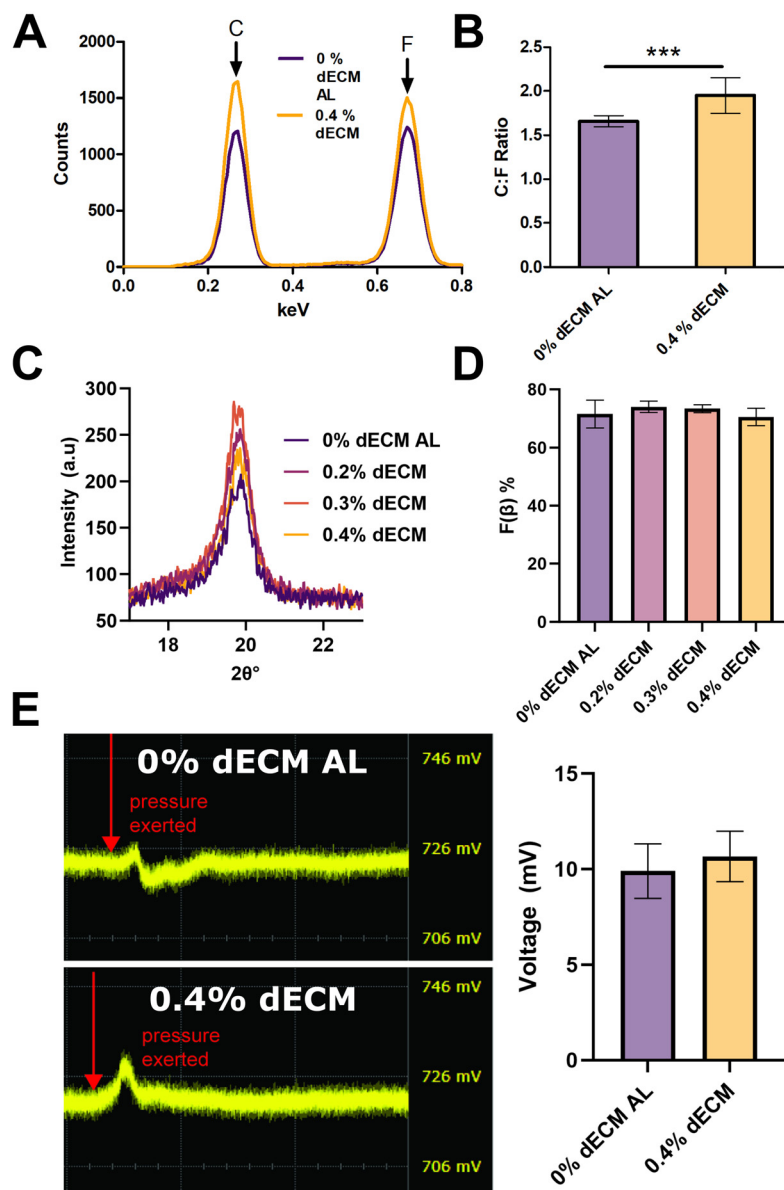
Fig. 3 Chemical and electrical properties of standard and blended scaffolds. (A) EDX analysis of the 0% and 0.4% dECM scaffolds showed the chemical spectrum of the material. (B) The carbon to fluorine ratio was measured using a ratio of atomic percentages. (C) XRD analysis detailing material crystallization of all scaffold types yielded 2θ measurements at approximately 19.8°, consistent with the β-phase conformation of PVDF-TrFE. (D) β-Phase percentages calculated from FTIR data show blended scaffolds maintained β-phase content similar to our PVDF-TrFE control. (E) Piezoelectric behavior (voltage changes in response to pressure) was preserved in the blended electrospinning process.

come disparities in fiber alignment. Overall, however, as time increased, so did cell growth. Aspect ratios of all groups were statistically higher at 24 h compared to 3 h.

3.4. *In vivo* implantation and tissue response

Scaffolds of PCL, 0% dECM PVDF-TrFE, and 0.4% dECM blended PVDF-TrFE were surgically implanted under the skin of adult male rats (Fig. S5). PCL scaffolds were chosen as a negative control due to their having FDA approval, common use already in medical devices, nonpiezoelectric nature, and the extensive rodent work already published that allow us to compare inflammatory profiles.[60–62] The 0.4% dECM scaffolds

had many favorable mechanical and biological characteristics which made it the optimal choice for implantation of our bio-functionalized scaffold groups.

In histological sections of tissue samples (Fig. 5A–C), scaffolds (denoted by black arrows) of each type did not appear morphologically different. Each group appeared to fold and curl on itself and where folding did occur, cell infiltration between folds was usually present (asterisks in Fig. 5A–C). Both scaffolds appeared to remain similar in thickness with no indications of material expansion that would lead to further irritation and inflammation of tissue.
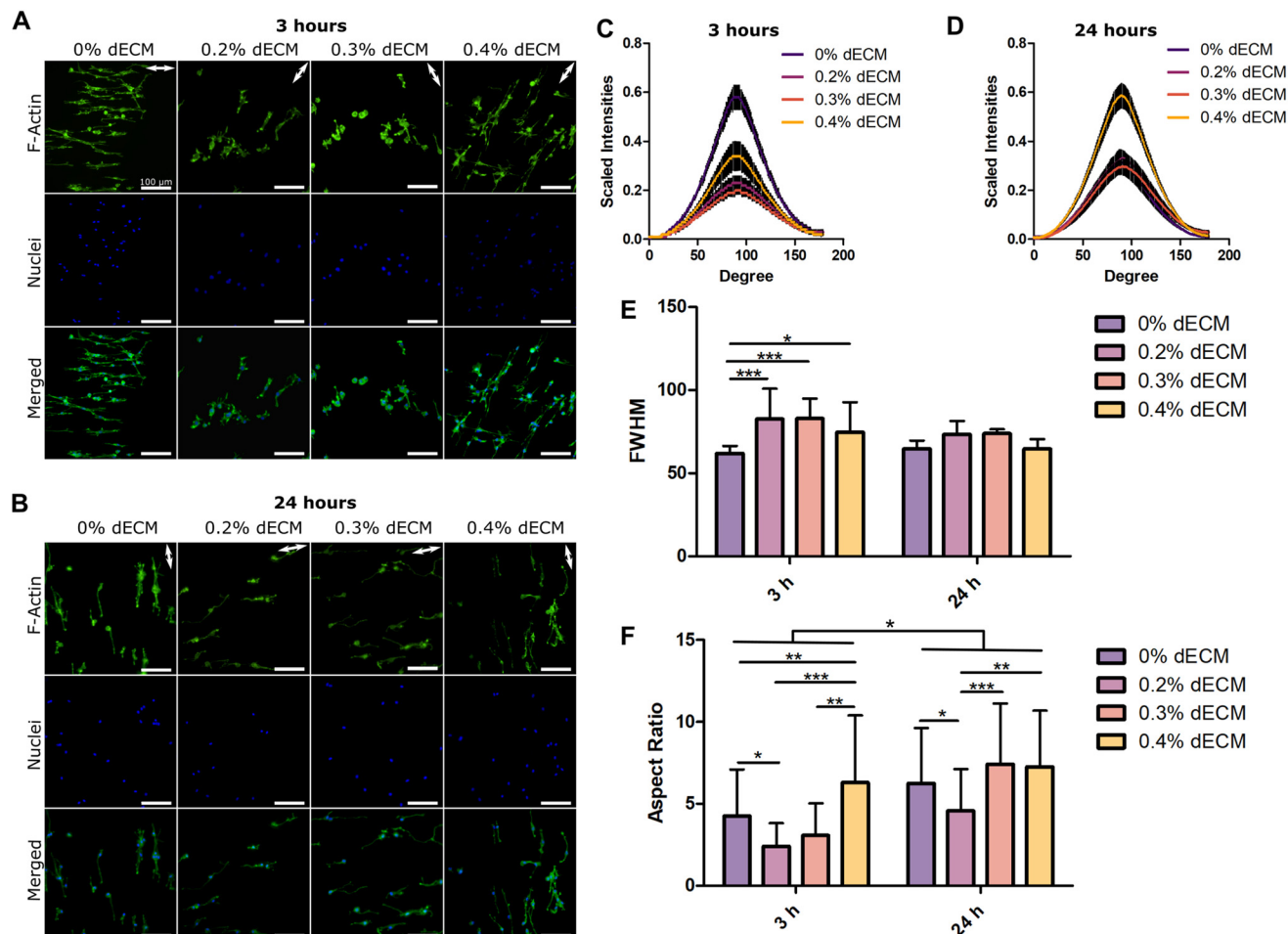
Fig. 4 Primary Schwann cell behavior *in vitro* on blend-electrospun PVDF-TrFE scaffolds. (A) After 3 hours, primary Schwann cells attached to all scaffolds and showed some alignment with the fiber direction. Scale bars are 100 μm. White arrows denote fiber direction. (B) After 24 hours, cells on all bioactive scaffolds again showed cell elongation and alignment. (C, D) Fourier transformed pixels of stained images at 3 h and 24 h, respectively were radially summed around 360 degrees providing cellular alignment intensities graphed from 0 to 180 degrees. Sharper peaks are indicative of greater alignment. (E) Full width-half maximum values (FWHM) were calculated for each curve at 3 h and 24 h. A larger value is indicative of less aligned cellular growth. No differences were observed between time points, but were observed between groups within time points. (F) Aspect ratios of cells were quantified at 3 and 24 h after plating. Some differences were observed between groups and there was a difference between time points. All data are *post-hoc p* values after a two-way ANOVA was significant and are reported as mean $\pm$ SD. * $p < 0.05$, ** $p < 0.01$, *** $p < 0.001$.

Scaffolds were assessed at 7 DPI for the formation of foreign body giant cells (FBGC) and fibrous capsule formation, both can indicate negative tissue reactions to the material (Table 1). When a material is implanted within the body, macrophages will surround the material in an effort to dissolve it. If the implant is not readily dissolved by a single macrophage these cells will fuse into a FBGC.[63] If a foreign body stimulates tissue irritation, then fibroblasts create a fibrous capsule that is characterized by dense collagen formation. The thickness and density of the collagen indicate the intensity of the tissue reaction. The host tissue remodeling response to PCL at 7 DPI was the creation of an accumulation of histiocytic macrophages (epithelioid cells) on the surface of the PCL, surrounded by immune cells, all characteristic of a mild foreign body granulomatous inflammation, with a paucity of FBGCs among the histiocytes on the surface of the material (Fig. 5A).

For PCL, a quantitative score of 3 (<1 macrophage per 40× field) was given for the very low numbers of FBGCs observed. Additionally, there was no evidence of dense collagenous capsule formation surrounding PCL scaffolds at 7 DPI (quantitative score = 3, total remodeling score = 3). The host tissue remodeling response to 0% PVDF-TrFE scaffolds was similar to that of PCL and minimal at 7 DPI (Fig. 5B). Slightly more FBGCs were observed, with an estimated score of 1 per 40× field (quantitative score = 2). Encapsulation formation in response to 0% dECM, PVDF-TrFE control scaffolds was non-existent (quantitative score = 3) yielding a total remodeling score of 2. This is, again, a very limited foreign body response. The host tissue remodeling response to 0.4% dECM PVDF-TrFE scaffolds was similar to the other scaffolds (Fig. 5C). Quantitatively, 0.4% dECM scaffolds presented with at least 1 FBGC aggregate per field (quantitative score = 2).
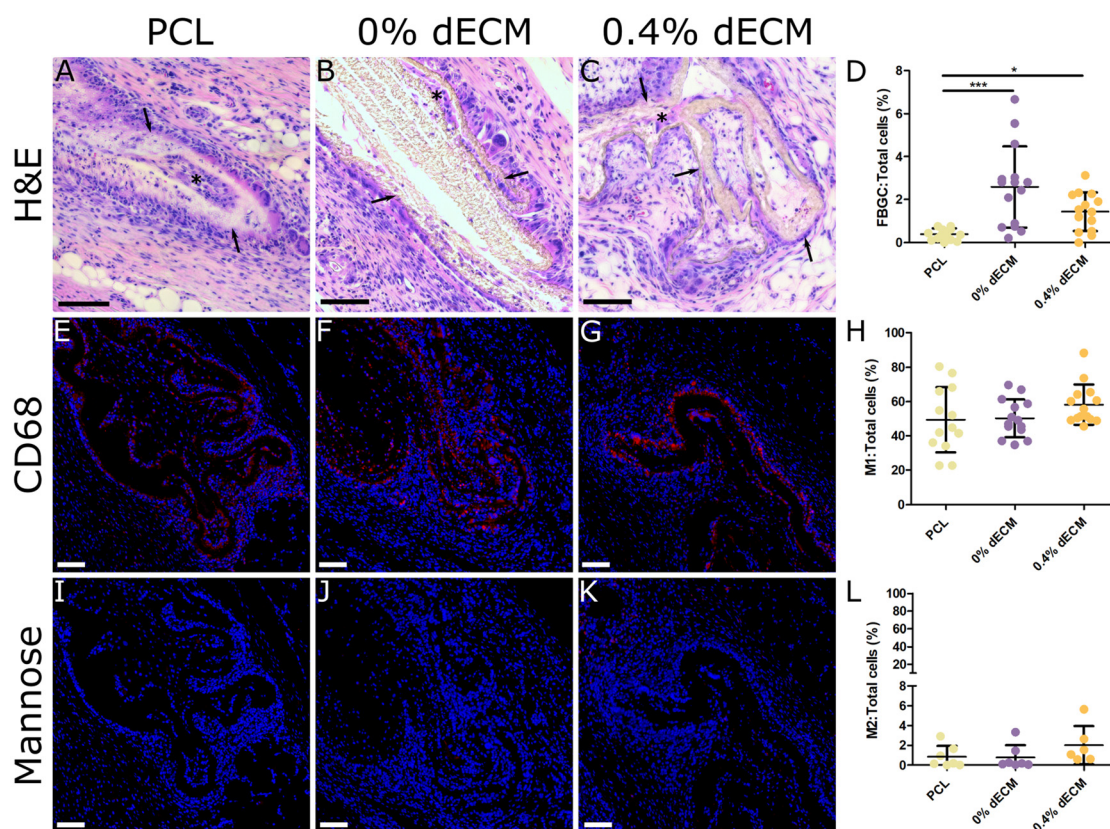
Fig. 5 Characterization of the host macrophage responses at 7 days post implantation. (A–C) In H&E-stained images of tissues surrounding PCL, 0% PVDF-TrFE, and 0.4% dECM scaffolds it was possible to see the accumulation of macrophages and FBGCs (arrows) on the scaffold surface and mild inflammation surrounding the scaffolds. Some clusters of cells and collagen were found within the scaffold material (asterisks). (D) The ratio of counted FBGCs to total number of cell nuclei within areas defined as containing inflammation provides a quantitative metric of the tissue reaction to the materials. (E–G) Immunofluorescent staining for M1 macrophage polarization types using anti-CD68 (red). (H) Total M1 macrophages measured as a ratio of M1 cells to total cells. (I–K) Immunofluorescent staining for M2 macrophages was done using an antibody against the mannose receptor (red). (L) Percentages of M2 macrophages were limited in all blended PVDF-TrFE scaffolds. Scale bars = 100 μm and numeric data are reported as mean $\pm$ SD. * $p < 0.05$, *** $p < 0.001$.

Table 1 Histological scoring as a metric of the foreign body response after 7 DPI. Higher scores represent a reconstructive response (see Table S2 for scale explanation). PCL offered the most favorable response in having fewer FBGCs, but all of the scaffold groups had moderately loose collagen around the material, showing no significant encapsulation after 7 days

	Multi-nucleated giant cells	Encapsulation	Remodeling aggregate score
PCL	3	3	3
0% PVDF-TrFE	2	3	2
0.4% PVDF-TrFE	2	3	2

Formation of fibrous capsules were absent (quantitative score = 3) giving the bioactive scaffolds a total remodeling score of 2.

To further analyze the tissue remodeling response at 7 DPI, a more detailed quantification was conducted to measure the number of FBGCs as a ratio to the total number of cells in the area of inflammation surrounding the implant. Scaffold images were subject to a counting threshold in ImageJ to yield total counts (Fig. S6). The ratio of FBGCs to total cells surrounding the scaffold was analyzed as a percentage and can be visualized in Fig. 5D. As was consistent with its remodeling score above, PCL implants expressed the lowest percentage of FBGCs (0.40%), and were significantly lower than the amounts for the 0.4% dECM scaffolds (1.43%) and the 0% dECM scaffolds (2.59%). While the 0% dECM average percentage was higher than 0.4% dECM, it was not significantly different. Thus, the base scaffold material stimulates more FBGCs than PCL and there is a suggestion that, if our numbers were increased, there might be an advantage of adding ECM.

3.5. Macrophage polarization surrounding scaffolds at 7 DPI

Macrophages are characterized across a spectrum of phenotypes depending on what signals activate them (classical or alternative stimuli) and what functions they perform when activated.[64] In the most simplistic classification scheme, however, they are treated as one of two ends of this spectrum: the classically activated, pro-inflammatory phenotype (M1) or the alternatively activated, pro-regenerative phenotype (M2).

For this study, macrophages were analyzed and identified as either M1 or M2 macrophages based on antibody staining for two specific macrophage protein markers, CD68 for M1 subtypes and the Mannose Receptor (CD206) for M2 subtypes. In a typical response to tissue injury or wounding, pro-inflammatory macrophage subtypes will arrive within the first 48 h of injury followed by an influx of pro-regenerative M2 macrophages as the cellular response shifts from the inflammation stage to the repair stage.[65] To examine this M1 response and potential shift towards an M2 response, implants were examined after an initial 7 d period.

At 7 d after implantation, a limited presence of the M1 subtype was noted in cells adjacent to PCL implants compared to the 0% dECM and 0.4% dECM blend (Fig. 5E–G). To quantify this, in designated ROI areas drawn around the area considered inflammatory (see Fig. S6), we measured the total area stained for M1 macrophages (CD68 staining) and expressed this as a percentage of the total number of cells (area of DAPI signal) (Fig. 5H). In each group, approximately half the cells surrounding the scaffold at 7 DPI were polarized towards the M1 phenotype, but there were no significant differences between the three scaffolds. This suggests that the three types of scaffolds elicited similar responses.

The M2 response was exceedingly limited at 7 DPI compared to the M1 response (Fig. 5I–K). The number of M2 macrophages was extremely low and there were no statistical differences in M2 presence between scaffold groups (Fig. 5L). Although still limited compared to the presence of M1 macrophages, there appeared to be more resident M2 macrophages surrounding the inflamed tissue area in areas farther than 133 μm away from our 0.4% scaffolds and outside our ROI areas (Fig. S7).

3.6. Immune response and scaffold appearance at 28 DPI

To analyze the progression of the host immune response to our scaffolds, we examined implants post-28 days, as shown in Fig. 6. At the time of sacrifice, all rats were reported to be healthy, did not express signs of discomfort, and all injury sites appeared fully healed and recovered. In sections stained with H&E, tissue responses to the scaffolds were very similar to those at 7 DPI. This is consistent with a continuation of a low-grade chronic (granulomatous) inflammation (two-sided maroon arrow in Fig. 6). This is characteristic of a mild host response to a biomaterial implant that may continue until the implant either dissolves or is passivated, i.e. by a dense capsule. Within the epithelioid macrophages directly on the surface of the implants, there were several FBGCs (arrow with triangle head, Fig. 6A–E). An issue with analyzing the 28-day results was that it was not possible to find the scaffold remnants in every sample and the amount of scaffold that was present was highly variable in size. When remnants of the scaffold were visible, there was no evidence of a significant increase in inflammation compared to 7 DPI, which speaks to the biocompatibility of our experimental scaffolds (Fig. 6). Uniquely in the 0% and 0.4% groups, but not the PCL group, in either sections without detectable scaffolds or adjacent to

remnants (Fig. 6C, bottom), there were areas that appeared disrupted compared to neighboring connective tissues. These areas contained irregular collagen, arterioles and venules (small but with several layers of smooth muscle, blue arrowheads in Fig. 6C), and small nerve fascicles (fascicles with multiple axons surrounded by an established perineurium, red arrowheads in Fig. 6C). These areas could have been remnants of the tissue reactions to a fully degraded scaffold or continued reaction to remaining small pieces of scaffold out of the plane of view. Significantly increased density of collagen and development of a thick capsule were not seen around either the scaffolds or these areas. Additional observations from our implants showed that existing close to the scaffolds or in adjacent tissues were an abundance of subcutaneous fat cells (Fig. 6, black arrow), consistent with similarly spun scaffold polymers also implanted beneath the skin. Over longer time periods (not tested) it will be important to monitor the extent and duration of chronic inflammation and characterize other long-term tissue responses to the remnants of PVDF-TrFE. PVDF-TrFE, so it is possible that, over time, the remnants might become a scar (an accumulation of a dense core of collagen), and a more significant capsule may develop that would separate this material from surrounding tissues. If the areas were to grow significantly over time, this could reduce motion or create further inflammation.[47]

4. Discussion

4.1. Blend-electrospun scaffolds incorporate physiological ECM

Blend electrospinning PVDF-TrFE and dECM proteins into a heterogenous scaffold forms a biomaterial capable of providing physical, electrical, and biochemical cues essential for desired cell behavior. Demonstrated here with SEM and EDX mapping, dECM was present throughout scaffolds as a coating on the fibers and as visible, web-like structures. This presence of proteins was confirmed by the increase in C : F ratio with the 0.4% versus the 0% scaffold (Fig. 3A and B). Fiber analysis showed that both the 0.2% and 0.4% dECM scaffolds had larger fiber diameters than the other groups, with 0.4% larger than 0.2%, and we attribute this increase to the addition of dECM content affecting solution viscosity. Fiber diameter is known to increase in the presence of more viscous solutions,[66,67] and when combining dECM and PVDF-TrFE, the viscosity of the precursor solution visibly increases, but not to a degree that causes adverse needle clogging, as noted by the absence of beading and fiber–fiber bonding in our SEM analysis.[68] Further studies would be required to decouple the relationship between dECM addition and viscosity; however, the importance of fiber diameters here is that fibers with micron-sized diameters (as seen with 0.2% and 0.4%) have been shown to improve neurite length and increase cell area.[69,70] The fact that the 0.4% scaffolds had the largest fiber diameters was one reason, among others, why this was chosen for in vivo experiments and that we propose might be the most
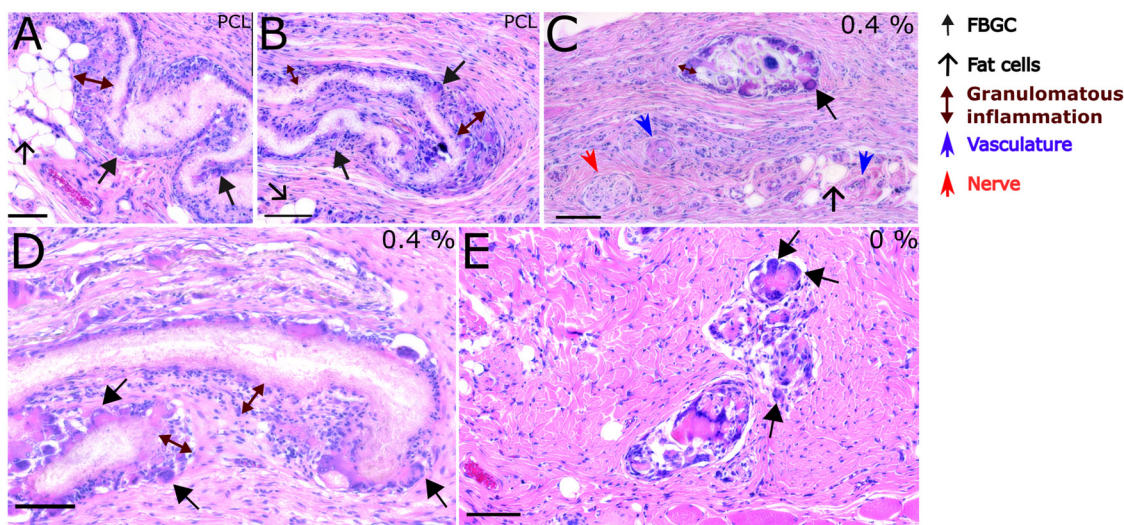
Fig. 6 Tissue samples were harvested and stained with H&E at 28 days post implantation. (A–E) Scaffold materials were identifiable in the PCL, 0% dECM, and 0.4% dECM groups and all displayed macrophages and FBGCs (triangle-headed arrows) at the implant surface and a surround of cell types characteristic of a mild foreign body granulomatous inflammation (two-sided maroon arrows), similar to that seen at 7 DPI. (C, E) The 0% and 0.4% samples occasionally had smaller amounts of identifiable scaffold material than with PCL, while all three scaffold types had similar amounts of collagenous tissue aligned around the implant. (C) The 0% (not shown) and 0.4% blended scaffolds, but not the PCL scaffolds displayed islands of disorganized collagen structure that contained aggregations of larger than capillary sized blood vessels (blue arrowheads) and small nerve fascicles (red arrowheads). These were found only adjacent to scaffold remnants or in areas where scaffold remnants had been expected. Fat cells (non-tri-angle-shaped black arrows) and were present close to all scaffold types. Scale bars = 100 μm.

advantageous among all tested here in a wound healing setting.

Fiber alignment in our piezoelectric biomaterial was chosen for two distinct reasons; it affects the overall piezoelectric capacity of the material and it helps facilitate directional cell growth and migration.[71] Through geometric confinement, aligned networks of nanofibers inherently align molecular dipoles within the polymer material to enhance polarization, thereby generating larger piezoelectric values.[71,72] 0.4% scaffolds showed the addition of dECM content still allows for the spinning of aligned fibers with bioactive material.

4.2. Mechanical properties of blended scaffolds are physiologically relevant

Bulk stiffness properties of the whole scaffold allow analysis of how the full scaffold compares with the stiffness of normal tissues. Our measurements in Fig. 2E showed that our 0.4% dECM scaffold had the highest Young's modulus of all groups. Additionally, the Young's modulus approached a value similar to that of a human peripheral nerve (~38 MPa).[57] This is advantageous because matching biomaterial stiffness to native tissue stiffness is important for long-term integration and managing the fibrotic response to implants.

The Young's modulus of individual fibers was also measured by nanoindentation analysis (Fig. 2F). This is a measure that shows the stiffness that cells are directly experiencing from the substrate. Here, all scaffold types differed from each other and 0.4% had the lowest stiffness (~50 kPa). Localized stiffness at the cellular level has been shown to direct cell shape, function and migration.[73–76] For instance,

macrophages interacting with substrates between 35 and 63 kPa stiffnesses were shown to shift towards the regenerative M2 phenotype in wound settings compared to substrates with softer stiffnesses near 3 kPa.[77]

The noticeable difference between increasing stiffness at the tissue level *versus* the reduced stiffness at the cellular level of the 0.4% scaffold, we hypothesize, is due to the complex relationship between fiber diameter and fiber alignment. Larger fibers are known to decrease fiber stiffness, but fiber orientation greatly enhances bulk stiffness of scaffolds at the tissue-like level when fibers are unidirectional aligned in the direction of stretching.[78,79]

4.3. Cell–biomaterial interactions were altered by the ECM content of scaffolds

In healthy tissue, the ECM is responsible for creating physical pathways for cell movement and interacting with growth factors and signal receptors to direct cell function.[10] At the onset of injury, cell–ECM communication becomes even more important as cell motility and phenotype are responsible for directing healing.[80] These cell–ECM interactions, mediated by transmembrane receptors known as integrins, sense forces exerted by their surrounding microenvironment that result in changes in cytoskeleton organization and contractility during migration, both of which are energy-intensive and closely associated with metabolic changes.[81,82] In a situation where cells have low adhesion to the ECM, a decrease in mitochondrial metabolism is seen.[83] The attachment assay at 3 h showed that the initial attachment and therefore presumably support of metabolism was greatest with the 0.3 and 0.4%

scaffolds, supporting our idea that the addition of the dECM is advantageous. A fibroblast cell line was chosen for initial testing due to the amount of ECM produced *in vitro*, as well as the high concentration of fibronectin, like seen in injuries. Moving forward, a natural next step is to use tissue specific cells to create dECM for certain applications.

The benefits of using aligned, nanofibrous scaffolds to enhance cell growth are well documented.[18,84–87] Cellular alignment is suspected to be a FAK-mediated mechanism by which downstream signaling cascades of RhoA kinase affect cellular elongation along the direction of the nanofibers.[85,86] Aspect ratio was greatest on 0.4% scaffolds at 3 h. We hypothesize the increase in aspect ratio is due to fiber diameter and dECM content. The presence of larger fibers and focal adhesion proteins in the dECM would be expected to prompt individual cell spreading along those fibers, thus exhibiting an elongated shape. This changed, however, at 24 h when aspect ratios on all scaffold groups increased, suggesting time is more influential on cells elongating along fibers than fiber diameter or dECM content. As cell alignment and adhesion are widely associated with regenerative behavior,[84,88–90] given our data to date, we cannot say for certain yet that our blended scaffolds demonstrate the ability to serve as a regenerative guide in a wound healing environment, but all scaffolds prompted elongated shapes in Schwann cells, which is a key regenerative phenotype in repair situations.

4.4. Blended Scaffolds with 0.4% dECM for implants

The 0.4% dECM scaffolds were chosen as the blended scaffold for *in vivo* implants due to their advantageous mechanical and biological characteristics. This group contained the highest proportion of micron-sized fiber diameters (Fig. 2B) and micron-sized fibers have been shown to improve neurite length and increase cell area.[69] The 0.4% scaffolds supported greater early cell attachment than 0% scaffolds (Fig. S4). Tissue-level stiffness of the 0.4% group was the only group closest to ideal nerve tissue values and stiffness at the cellular level of this group was also the only scaffold group to have ideal cell-level stiffness (~50 kPa) where macrophages have been shown to promote M2 phenotypes (~60 kPa).[77] Biologically, we showed cells on 0.4% scaffolds demonstrated aligned growth after 24 h and larger aspect ratios than scaffolds without protein at 3 h and larger than 0.2% scaffolds at 24 h, which is a desired morphology in the regenerative Schwann cell phenotype.

4.5. Tissue inflammation and macrophage response to scaffolds

Our observations of implanted scaffolds at 7 DPI show that there was minimal inflammation occurring and that M1 macrophages accumulated at the edges of the implants comprising between 50 and 60% of cells. The lack of much larger pockets of M1 macrophages is good and the accumulation of M1 macrophages is normal for 7 days after a wound injury to the skin.[63] Interestingly, there were no differences in the amount of M1 macrophages between the FDA-approved

PCL and the 0% and 0.4% scaffolds over the PCL. There were slight differences in numbers of quantifiable FBGCs, with both the 0% and 0.4% scaffolds having increases relative to PCL. This suggests that the electrospun PVDF-TrFE material might cause a minor increase in immune responses. This might reflect the fact that the PVDF-TrFE material in the scaffold is not biodegradable, while PCL is well-known to be degradable. Another possible explanation may be the electroactive nature of the piezoelectric scaffold. Although not the primary factor, electrical stimulation is an additional variable thought to play a role in FBGC formation.[91] There might have been a trend towards fewer FBGCs with 0.4% (Fig. 5D), so further studies exploring either higher contents of dECM or a combination of ECM proteins to overcome this slight difference are needed to confirm this hypothesis. In the literature, it is known that implanted medical devices coated with fibronectin and fibrinogen form lower numbers of FBGCs compared to uncoated implants,[92] suggesting our blended scaffolds may replicate a native cell environment. Adverse and foreign responses in the immune response progression would show as a robust and organized fibrous capsule, not constructive remodeling.[93] Although no robust encapsulation was present after 28 d, extending these studies past 28 d might provide a clearer picture of encapsulation surrounding our implants.

No differences in the M1 or M2 macrophage response were seen across scaffold groups at 7 DPI, suggesting there is no negative effect of the piezoelectric component or dECM component of the PVDF-TrFE material. Because the M2 response was limited in all groups, it is suspected 7 DPI was either too short or too long of a period to visualize the influx of proregenerative M2 macrophages. A time point of 7 DPI might represent the entire M1 response, but a wave of M2 macrophages may only appear after the implant has been degraded to complete the tissue repair process, which becomes difficult to analyze in polymer scaffolds with extremely slow degradation rates.

4.6. Tissue appearance and capsule formation at 28 DPI

Implants that are not completely phagocytized through the initial phases of the immune reaction lead to an increase in fibroblast activity.[47] Fibroblasts deposit collagen that forms bands around the implant to encapsulate the implant and separate it from other tissues. If the implant persists and the collagenous capsule is not resorbed or reduced, this tissue can become scar tissue.[87,94] Our implant showed limited capsule formation surrounding our scaffolds overall. This is indicative of a reduced foreign body response, at least at 7 and 28 DPI. This is consistent with previous studies where dECM added to nanofibrous scaffolds improved cellular alignment, proliferation, and the secretion of actin and focal adhesion genes of fibroblasts *in vitro* after 4 d and showed regenerative-like promise compared to PCL scaffolds *in vivo* after 14 d.[95]

Following fibroblast proliferation and migration, neovascularization begins *via* the sprouting of new small blood vessels from preexisting vasculature in the surrounding area in a constructive remodeling response.[95,96] While not consistent with

an angiogenic environment, seen in our study was an accumulation of small arterioles and venules neighboring our 0.4% dECM scaffolds. Previous *in vitro* findings have shown electrical stimulation of endothelial cells activates the NOS pathway and upregulates FGF2 which activates the MAPK/ERK pathway and promotes VEGF expression.[17,97] Although future studies past the 28-day mark detailing *in vivo* electrical currents emanating from our scaffolds would be required to confirm this, the electrical activity in our PVDF-TrFE scaffolds may have some effect in the presence of this vasculature. Deformations in the piezoelectric scaffold due to natural movement in the tissue might have activated the electrical activity required to alter endothelial cell growth.

It is also known there is a strong connection between the nervous system and the skin involving various cytokines that promote nerve integration during advanced stages of wound healing.[98,99] While further research would be required to isolate and identify the neuromodulatory and cytokine behavior involved, it is well known electrical activity accelerates the wound healing process and facilitates optimal axonal regrowth.[24,27,31,36] Hence, we believe the increased presence of nerves surrounding our wound area is potentially attributed to the electrical activity emerging from our piezoelectric scaffolds, which would be exciting if it held true in another study with larger numbers of animals and with a more expanded time scale than 28 d.

4.7. Clinical relevance of blended scaffolds

Our findings provide a method to fabricate a scaffold capable of being manipulated into a nerve guidance conduit that merges the necessary requirements to promote functional recovery over extended nerve gap injuries. Directional growth from aligned structures, electrical cues from piezoelectric nanofibers (that could be noninvasively stimulated), and biochemical cues from native, whole decellularized extracellular matrix were bulk functionalized into a single engineered material that might be capable of promoting enhanced nerve regeneration. Our previous work has shown PVDF-TrFE can be electrospun into aligned nanofibrous conduits capable of retaining their piezoelectric potential.[17] We have expanded upon this with a blended precursor solution that could introduce additional chemical and substrate cues directly involved with jump-starting Schwann cell and epithelial cell migration that might be capable of nurturing healthy and essential cell and neuronal growth, while reducing negative host immune responses.

5.   Conclusion

Conventional biomaterial implants for tissue repair are often limited by poor immunological compatibility and insufficient support for regenerative healing. To overcome these challenges, we developed a piezoelectric scaffold composed of PVDF-TrFE, functionalized with cell-derived decellularized extracellular matrix (dECM) to deliver integrated physical, elec-

trical, and biochemical cues. Electrospun into aligned fibers mimicking native ECM architecture, these scaffolds were evaluated through *in vitro* and early *in vivo* studies to assess their potential as a biomaterial geared towards tissue engineering applications.

Our findings demonstrate that this streamlined biofunctionalization approach yields scaffolds that are non-cytotoxic, support pro-regenerative cellular responses, and exhibit the capacity to modulate the immune environment favorably. The combination of structural mimicry, piezoelectric signaling, and ECM-derived biochemical functionality positions these scaffolds as promising candidates for future tissue repair applications, particularly in the peripheral nervous system.

Conflicts of interest

The authors declare that they have no disclosures to report that could have influenced the work reported in this paper.

Data availability

The raw data were generated at the University of Cincinnati. The main data supporting this article has also been included as part of the SI. See DOI: **https://doi.org/10.1039/d5bm01054c**.

Upon reasonable request, any other data supporting the findings contained within this study are available from the corresponding author.

Acknowledgements

References

1 S. Yegiyants, D. Dayicioglu, G. Kardashian and Z. J. Panthaki, *J. Craniofac. Surg.*, 2010, **21**, 998.

2 M. Heiland, R. Smeets, A. Henningsen, C. Knipfer, R. Gaudin and T. Hadlock, *BioMed Res. Int.*, 2016, **2016**, 1.

3 S. Yi, Y. Zhang, X. Gu, L. Huang, K. Zhang, T. Qian and X. Gu, *Burns Trauma*, 2020, **8**, tkaa002.

4 M. C. Dodla and R. V. Bellamkonda, *Biomaterials*, 2008, **29**, 33.

5   R. A. Neal, S. G. McClugage, M. C. Link, L. S. Sefcik, R. C. Ogle and E. A. Botchwey, *Tissue Eng., Part C*, 2009, **15**, 11.

6   S. Nagam Hanumantharao, N. Alinezhadbalalami, S. Kannan, M. Friske and S. Rao, *RSC Adv.*, 2019, **9**, 40190.

7   M. C. Chen, Y. C. Sun and Y. H. Chen, *Acta Biomater.*, 2013, **9**, 5562.

8   S. H. Ku, S. H. Lee and C. B. Park, *Biomaterials*, 2012, **33**, 6098.

9   C. S. Smith, J. A. Orkwis, A. E. Bryan, Z. Xu and G. M. Harris, *Eur. J. Cell Biol.*, 2022, **101**, 151277.

10 Z. Xu, J. A. Orkwis, B. M. DeVine and G. M. Harris, *J. Tissue Eng. Regen. Med.*, 2020, **14**, 229.

11 Z. Xu, J. A. Orkwis and G. M. Harris, *Int. J. Mol. Sci.*, 2021, **22**, 4821.

12 J. A. Gomez-Sanchez, K. S. Pilch, M. van der Lans, S. V. Fazal, C. Benito, L. J. Wagstaff, R. Mirsky and K. R. Jessen, *J. Neurosci.*, 2017, **37**, 9086.

13 K. R. Jessen and P. Arthur-Farraj, *Glia*, 2019, **67**, 421.

14 C. Bonnans, J. Chou and Z. Werb, *Nat. Rev. Mol. Cell Biol.*, 2014, **15**, 786.

15 M. A. Chernousov, W.-M. Yu, Z.-L. Chen, D. J. Carey and S. Strickland, *Glia*, 2008, **56**, 1498.

16 G. M. Harris, N. N. Madigan, K. Z. Lancaster, L. W. Enquist, A. J. Windebank, J. Schwartz and J. E. Schwarzbauer, *Matrix Biol.*, 2017, **60–61**, 176.

17 J. A. Orkwis, A. K. Wolf, Z. J. Mularczyk, A. E. Bryan, C. S. Smith, R. Brown, M. Krutko, A. McCann, R. M. Collar, L. Esfandiari and G. M. Harris, *Biomater. Adv.*, 2022, **140**, 213081.

18 J. A. Orkwis, A. K. Wolf, S. M. Shahid, C. Smith, L. Esfandiari and G. M. Harris, *Macromol. Biosci.*, 2020, **20**, e2000197.

19 A. H. Rajabi, M. Jaffe and T. L. Arinzeh, *Acta Biomater.*, 2015, **24**, 12.

20 S. Wu, M.-S. Chen, P. Maurel, Y. Lee, M. B. Bunge and T. L. Arinzeh, *J. Neural Eng.*, 2018, **15**, 56010.

21 A. E. Bryan, M. Krutko, J. Westphal, M. Sheth, L. Esfandiari and G. M. Harris, *Mil. Med.*, 2023, **188**, 61.

22 J. A. Westphal, A. E. Bryan, M. Krutko, L. Esfandiari, S. C. Schutte and G. M. Harris, *Biomimetics*, 2023, **9**, DOI: **10.3390/biomimetics9010002**.

23 M. Krutko, H. M. Poling, M. Sheth, S. Kongsomros, A. E. Bryan, M. Sharma, A. Singh, H. A. Reza, K. A. Wikenheiser-Brokamp, T. Takebe, M. A. Helmrath, G. M. Harris and L. Esfandiari, *Adv. Mater. Technol.*, 2025, e01513, DOI: **10.1002/admt.202401513**.

24 A. N. Koppes, A. L. Nordberg, G. M. Paolillo, N. M. Goodsell, H. A. Darwish, L. Zhang and D. M. Thompson, *Tissue Eng., Part A*, 2014, **20**, 494.

25 Z. Liang, T. Lei, S. Wang, Z. Luo and X. Hu, *BioTechniques*, 2019, **67**, 11.

26 A. A.-M. Abdulhakeem, *J. Neurosci.*, 2000, **20**, 2602.

27 X. Li, T. Zhang, C. Li, W. Xu, Y. Guan, X. Li, H. Cheng, S. Chen, B. Yang, Y. Liu, Z. Ren, X. Song, Z. Jia, Y. Wang and J. Tang, *Glia*, 2023, **71**, 758.

28 T. Gordon, O. Sulaiman and J. G. Boyd, *J. Peripher. Nerv. Syst.*, 2003, **8**, 236.

29 J. Jacob, N. More, K. Kalia and G. Kapusetti, *Inflammation Regener.*, 2018, **38**, 2.

30 Y. S. Lee and T. L. Arinzeh, *Tissue Eng., Part A*, 2012, **18**, 2063.

31 B. Reid and M. Zhao, The Electrical Response to Injury: Molecular Mechanisms and Wound Healing, *Adv. Wound Care*, 2014, **3**, 184–201.

32 A. Casella, A. Panitch and J. K. Leach, *Bioelectricity*, 2021, **3**, 27.

33 J. Song, Z. Yuan, X. Yu, Y. Shen, J. Wu, B. Sun, C. X. Qin, M. El-Newehy, X. Mo and H. Gu, *Burns Trauma*, 2025, **13**, tkaf039.

34 L. Wu, H. Gao, Q. Han, W. Guan, S. Sun, T. Zheng, Y. Liu, X. Wang, R. Huang and G. Li, *Biomater. Sci.*, 2023, **11**, 7296.

35 S. F. Albert and E. Wong, *Clin. Podiatr. Med. Surg.*, 1991, **8**, 923.

36 R. Luo, J. Dai, J. Zhang and Z. Li, *Adv. Healthcare Mater.*, 2021, **10**, e2100557.

37 Y. Wu, J. Zou, K. Tang, Y. Xia, X. Wang, L. Song, J. Wang, K. Wang and Z. Wang, *Burns Trauma*, 2024, **12**, tkae013.

38 J. Fang, L. Nan, K. Song, Z. Weng, J. Shan, V. Shahin, J. Liu and Y. Qian, *Adv. Technol. Neurosci.*, 2024, **1**, 43.

39 B. Bakhshandeh, N. Ranjbar, A. Abbasi, E. Amiri, A. Abedi, M. Mehrabi, Z. Dehghani and C. P. Pennisi, *Bioeng. Transl. Med.*, 2023, **8**, e10383.

40 V. L. Albaugh, K. Mukherjee and A. Barbul, *J. Nutr.*, 2017, **147**, 2011.

41 S.-T. Jiang, W.-J. Chuang and M.-J. Tang, *Kidney Int.*, 2000, **57**, 1860.

42 S. Suri and C. E. Schmidt, *Tissue Eng., Part A*, 2010, **16**, 173.

43 S. Suri, L. Han, W. Zhang, A. Singh, S. Chen and C. E. Schmidt, *Biomed. Microdevices*, 2011, **13**, 983.

44 Y. Asawa, T. Sakamoto, M. Komura, M. Watanabe, S. Nishizawa, Y. Takazawa, T. Takato and K. Hoshi, *Cell Transplant.*, 2012, **21**, 1431.

45 A. P. Khandwekar, D. P. Patil, A. A. Hardikar, Y. S. Shouche and M. Doble, *J. Biomed. Mater. Res., Part A*, 2010, **95**, 413.

46 B. Veleirinho, D. S. Coelho, P. F. Dias, M. Maraschin, R. Pinto, E. Cargnin-Ferreira, A. Peixoto, J. A. Souza, R. M. Ribeiro-do-Valle and J. A. Lopes-da-Silva, *PLoS One*, 2014, **9**, e95293.

47 J. M. Anderson and S. Jiang, in *The Immune Response to Implanted Materials and Devices: The Impact of the Immune System on the Success of an Implant*, ed. B. Corradetti, Springer International Publishing, Cham, 2017, pp. 15–36.

48 G. M. Harris, I. Raitman and J. E. Schwarzbauer, in *Methods in Cell Biology*, ed. R. P. Mecham, Academic Press, 2018, pp. 97–114.

49 D. O. Freytes, J. Martin, S. S. Velankar, A. S. Lee and S. F. Badylak, *Biomaterials*, 2008, **29**, 1630.

50 Y.-S. Lee and T. L. Arinzeh, *Polymers*, 2011, **3**, 413.

51 K. Yu Wang, T.-S. Chung and M. Gryta, *Chem. Eng. Sci.*, 2008, **63**, 2587.

52 I. N. Sneddon, *Int. J. Eng. Sci.*, 1965, **3**, 47.

53 B. N. Brown, R. Londono, S. Tottey, L. Zhang, K. A. Kukla, M. T. Wolf, K. A. Daly, J. E. Reing and S. F. Badylak, *Acta Biomater.*, 2012, **8**, 978.

54 R. Dorati, E. Chiesa, S. Pisani, I. Genta, T. Modena, G. Bruni, C. R. M. Brambilla, M. Benazzo and B. Conti, *J. Drug Delivery Sci. Technol.*, 2020, **58**, 101781.

55 A. S. Motamedi, H. Mirzadeh, F. Hajiesmaeilbaigi, S. Bagheri-Khoulenjani and M. Shokrgozar, *Prog. Biomater.*, 2017, **6**, 113.

56 N. Alharbi, A. Brigham and M. Guthold, *Nanomaterials*, 2023, **13**, 1359.

57 C. F. Guimarães, L. Gasperini, A. P. Marques and R. L. Reis, *Nat. Rev. Mater.*, 2020, **5**, 351.

58 N. Weber, Y.-S. Lee, S. Shanmugasundaram, M. Jaffe and T. L. Arinzeh, *Acta Biomater.*, 2010, **6**, 3550.

59 T. Lei, X. Cai, X. Wang, L. Yu, X. Hu, G. Zheng, W. Lv, L. Wang, D. Wu, D. Sun and L. Lin, *RSC Adv.*, 2013, **3**, 24952.

60 U. Adhikari, X. An, N. Rijal, T. Hopkins, S. Khanal, T. Chavez, R. Tatu, J. Sankar, K. J. Little, D. B. Hom, N. Bhattarai and S. K. Pixley, *Acta Biomater.*, 2019, **98**, 215.

61 D. Castellano, M. Blanes, B. Marco, I. Cerrada, A. Ruiz-Saurí, B. Pelacho, M. Araña, J. A. Montero, V. Cambra, F. Prosper and P. Sepúlveda, *Stem Cells Dev.*, 2014, **23**, 1479.

62 L. Zhao, X. Li, L. Yang, L. Sun, S. Mu, H. Zong, Q. Li, F. Wang, S. Song, C. Yang, C. Zhao, H. Chen, R. Zhang, S. Wang, Y. Dong and Q. Zhang, *Mater. Sci. Eng., C*, 2021, **118**, 111441.

63 J. M. Anderson, in *Principles of Regenerative Medicine*, ed. A. Atala, R. Nerem, R. Lanza, A. Atala, A. G. Mikos, R. Lanza, R. Nerem and T. Mikos, Elsevier Science & Technology, United States, 2019, pp. 675–694.

64 M. Scatena, K. V. Eaton, M. F. Jackson, S. A. Lund and C. M. Giachelli, in *The Immune Response to Implanted Materials and Devices: The Impact of the Immune System on the Success of an Implant*, ed. B. Corradetti, Springer International Publishing, Cham, 2017, pp. 37–62.

65 J. M. Reinke and H. Sorg, *Eur. Surg. Res.*, 2012, **49**, 35.

66 R. M. Nezarati, M. B. Eifert and E. Cosgriff-Hernandez, *Tissue Eng., Part C*, 2013, **19**, 810.

67 B. Cramariuc, R. Cramariuc, R. Scarlet, L. R. Manea, I. G. Lupu and O. Cramariuc, *J. Electrost.*, 2013, **71**, 189.

68 K. Kanjanapongkul, S. Wongsasulak and T. Yoovidhya, *J. Appl. Polym. Sci.*, 2010, **118**, 1821.

69 H. B. Wang, M. E. Mullins, J. M. Cregg, C. W. McCarthy and R. J. Gilbert, *Acta Biomater.*, 2010, **6**, 2970.

70 C. A. Bashur, L. A. Dahlgren and A. S. Goldstein, *Biomaterials*, 2006, **27**, 5681.

71 V. Cauda, S. Stassi, K. Bejtka and G. Canavese, *ACS Appl. Mater. Interfaces*, 2013, **5**, 6430.

72 C. Chang, V. H. Tran, J. Wang, Y.-K. Fuh and L. Lin, *Nano Lett.*, 2010, **10**, 726.

73 G. M. Harris, M. E. Piroli and E. Jabbarzadeh, *Adv. Funct. Mater.*, 2014, **24**, 2396.

74 G. M. Harris, T. Shazly and E. Jabbarzadeh, *PLoS One*, 2013, **8**, 81113.

75 J. Fu, Y.-K. Wang, M. T. Yang, R. A. Desai, X. Yu, Z. Liu and C. S. Chen, *Nat. Methods*, 2010, **7**, 733.

76 D. E. Discher, P. Janmey and Y. Wang, *Science*, 2005, **310**, 1139.

77 M. Chen, Y. Zhang, P. Zhou, X. Liu, H. Zhao, X. Zhou, Q. Gu, B. Li, X. Zhu and Q. Shi, *Bioact. Mater.*, 2020, **5**, 880.

78 D. Alexeev, N. Goedecke, J. Snedeker and S. Ferguson, *Mater. Today Commun.*, 2020, **24**, 101211.

79 M. M. Maciel, S. Ribeiro, C. Ribeiro, A. Francesko, A. Maceiras, J. L. Vilas and S. Lanceros-Méndez, *Composites, Part B*, 2018, **139**, 146.

80 F. Gonzalez-Perez, E. Udina and X. Navarro, in *International Review of Neurobiology*, ed. S. Geuna, I. Perroteau, P. Tos and B. Battiston, Academic Press, 2013, pp. 257–275.

81 Y. Wu, M. R. Zanotelli, J. Zhang and C. A. Reinhart-King, *Biophys. J.*, 2021, **120**, 1705.

82 J. D. Hood and D. A. Cheresh, *Nat. Rev. Cancer*, 2002, **2**, 91.

83 E. Crosas-Molist, V. Graziani, O. Maiques, P. Pandya, J. Monger, R. Samain, S. L. George, S. Malik, J. Salise, V. Morales, A. Le Guennec, R. A. Atkinson, R. M. Marti, X. Matias-Guiu, G. Charras, M. R. Conte, A. Elosegui-Artola, M. Holt and V. Sanz-Moreno, *Nat. Commun.*, 2023, **14**, 2740.

84 W. Wang, S. Itoh, K. Konno, T. Kikkawa, S. Ichinose, K. Sakai, T. Ohkuma and K. Watabe, *J. Biomed. Mater. Res., Part A*, 2009, **91**, 994.

85 M. N. Andalib, J. S. Lee, L. Ha, Y. Dzenis and J. Y. Lim, *Biochem. Biophys. Res. Commun.*, 2016, **473**, 920.

86 M. N. Andalib, J. S. Lee, L. Ha, Y. Dzenis and J. Y. Lim, *Acta Biomater.*, 2013, **9**, 7737.

87 T. Fee, S. Surianarayanan, C. Downs, Y. Zhou and J. Berry, *PLoS One*, 2016, **11**, e0154806.

88 S. Hoehme, M. Brulport, A. Bauer, E. Bedawy, W. Schormann, M. Hermes, V. Puppe, R. Gebhardt, S. Zellmer, M. Schwarz, E. Bockamp, T. Timmel, J. G. Hengstler and D. Drasdo, *Proc. Natl. Acad. Sci. U. S. A.*, 2010, **107**, 10371.

89 S. Y. Chew, R. Mi, A. Hoke and K. W. Leong, *Biomaterials*, 2008, **29**, 653.

90 B. Etemad-Moghadam, S. Guo and K. J. Kemphues, *Cell*, 1995, **83**, 743.

91 M. T. Rahman, D. A. Chari, G. Ishiyama, I. Lopez, A. M. Quesnel, A. Ishiyama, J. B. Nadol and M. R. Hansen, *Hear. Res.*, 2022, **422**, 108536.

92 M. Shen, I. Garcia, R. V. Maier and T. A. Horbett, *J. Biomed. Mater. Res., Part A*, 2004, **70**, 533.

93 M. E. Scarritt, R. Londono and S. F. Badylak, Host Response to Implanted Materials and Devices: An Overview, in *The Immune Response to Implanted Materials and Devices*, ed. B. Corradetti, Springer, Cham, 2017, DOI: 10.1007/978-3-319-45433-7_1.

94 N. S. Sharma, A. Karan, H. Q. Tran, J. V. John, S. M. Andrabi, S. M. Shatil Shahriar and J. Xie, *Acta Biomater.*, 2024, **184**, 81.

95 L. L. Nguyen and P. A. D'Amore, *Int. Rev. Cytol.*, 2001, **204**, 1.

96 T. Browder, J. Folkman and S. Pirie-Shepherd, *J. Biol. Chem.*, 2000, **275**, 1521.

97 H. Bai, J. V. Forrester and M. Zhao, *Cytokine*, 2011, **55**, 110.

98 B. Brazzini, I. Ghersetich, J. Hercogova and T. Lotti, *Dermatol. Ther.*, 2003, **16**, 123.

99 A. S. Mehta, S. Teymoori, C. Recendez, D. Fregoso, A. Gallegos, H.-Y. Yang, E. Aslankoohi, M. Rolandi, R. R. Isseroff, M. Zhao and M. Gomez, *Sci. Rep.*, 2023, **13**, 16885.